Chapter 4
OpenPET Enabling PET Imaging During Radiotherapy

Taiga Yamaya and Hideaki Tashima

Abstract The OpenPET is the world's first open-type 3D PET scanner for PET image-guided particle therapy such as in situ dose verification and direct tumor tracking. The key technology, which enabled the OpenPET realization, is a depth-of-interaction detector. Even with a full-ring geometry, the OpenPET has an open gap between its two detector rings through which the treatment beam passes. Following the initial proposal of the dual-ring OpenPET (DROP), a small prototype was developed to show a proof of concept. The single-ring OpenPET (SROP) was also proposed as a more efficient geometry than DROP in terms of manufacturing, cost, and sensitivity. A small SROP prototype was developed, and feasibility of visualizing a 3D distribution of beam stopping positions inside a phantom was shown with the help of radioisotope particle beams, used as primary beams. Following these results, a full-size whole-body DROP prototype was developed.

Keywords PET • Particle therapy • Depth of interaction (DOI) • Image-guided radiotherapy • IGRT

4.1 Introduction

Cancer is a major cause of death in developed nations, and the disease death rate continues to increase. Therefore, many efforts have been made toward better diagnosis and better treatment. Among diagnostic tools, positron emission tomography (PET), which can visualize functions such as metabolism by injecting radioisotope tracers labeled with positron emitters, is expected to enable earlier and more precise cancer diagnosis. However, big improvements of PET could still be made, including spatial resolution, sensitivity, and manufacturing costs. For example, the sensitivity of present PET scanners does not exceed 10%, and thus, more than 90% of the gamma rays emitted from a patient are not utilized for imaging.

T. Yamaya (✉) • H. Tashima
National Institute of Radiological Sciences (NIRS), National Institutes for Quantum and Radiological Science and Technology (QST), Chiba, Japan
e-mail: yamaya.taiga@qst.go.jp; tashima.hideaki@qst.go.jp

T. Inoue et al. (eds.), *Personalized Pathway-Activated Systems Imaging in Oncology*, DOI 10.1007/978-981-10-3349-0_4

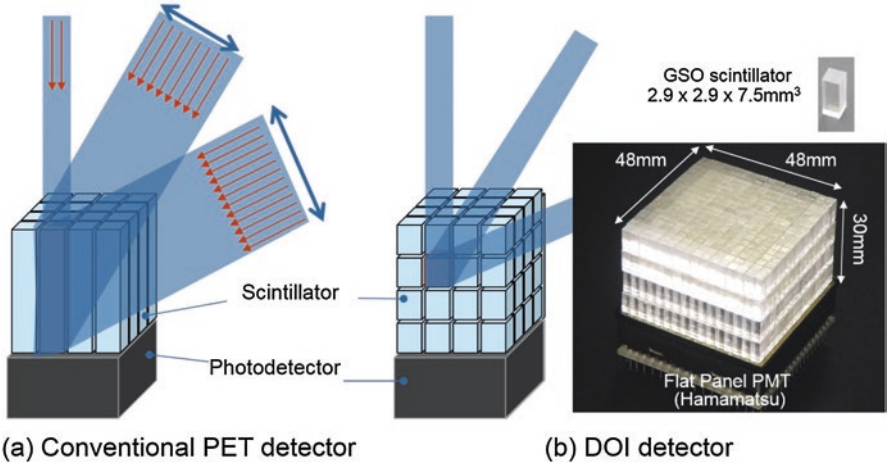

Fig. 4.1 Shows the comparison between a conventional PET detector (**a**) and the depth-of-interaction (DOI) detector (**b**). The DOI detector eliminates the parallax error, caused by the thickness of the crystals in conventional detectors

A depth-of-interaction (DOI) detector, for which various positioning methods have been studied [1–7], will be a key device to get any significant improvement in sensitivity while maintaining high spatial resolution (Fig. 4.1). In order to maintain enough detection efficiency, the scintillation crystals should be 2–3 cm long. In conventional detectors, the crystal thickness causes uncertainty in position identification, which results in degraded spatial resolution at the peripheral area of a field of view (FOV). On the other hand, the DOI detector can reduce the parallax error while maintaining the efficiency.

Figure 4.1b shows a four-layered DOI detector based on a light sharing method [8, 9], one of the successful proofs of concept made for the jPET-D4, which is a brain prototype PET system with the DOI detectors. It has a nearly uniform spatial resolution of around 2 mm all over the FOV, which was obtained using iterative image reconstruction with the geometrically defined system matrix [10]. This detector has been upgraded to get better spatial resolution at lower production costs. Moreover, the successful identification by the 32 × 32 × 4 array of LYSO crystals ($1.45 \times 1.45 \times 4.5$ mm^3 in size) with a 64channel flat panel PMT (H8500, Hamamatsu Photonics K.K., Japan) [11] is the base for Shimadzu's new positron emission mammography products [12].

For treatment, on the other hand, radiotherapy is essential for effective cancer treatment with minimized side effects. Specifically, particle therapy such as proton and carbon ion therapy are expected to be the ultimate radiotherapy because they can concentrate the dose even in a deep tumor. Thus, there has been remarkable progress in PET and radiotherapy, but no one has looked into the great potential to be obtained by the combination of both.

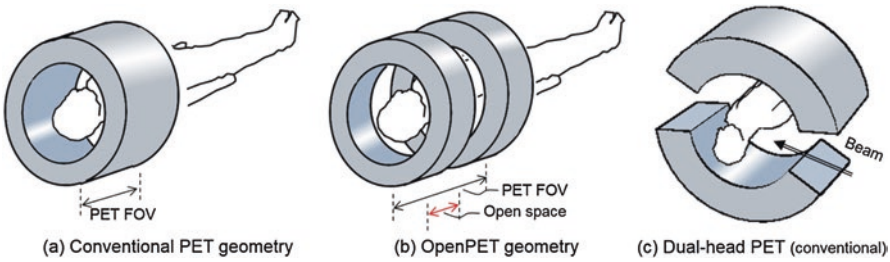

Fig. 4.2 Provides examples of a PET geometry: (**a**) a typical cylindrical PET geometry, (**b**) the OpenPET geometry, and (**c**) a dual-head PET geometry which has been proposed for in-beam PET

An open-type PET geometry (OpenPET) is a new idea to visualize a physically opened space between two detector rings [13], which will move researchers toward a future joint PET imaging and radiotherapy system. OpenPET is expected to achieve in-beam PET, which is a method to monitor in situ charged particle therapy. Without injecting any PET tracer, positron emitters are produced through fragmentation reactions between the projectiles and the atomic nuclei of the tissue during patient irradiation [14]. Compared with conventional radiation therapy, charged particle therapy can highly concentrate the dose in a tumor. This means if there is any difference between the actual irradiation and the treatment plan, the tumor treatment will be compromised, and the normal tissue around the tumor will be damaged. Therefore, quality of treatment must be assured for in-beam PET.

Dual-head PET cameras have been developed at the Gesellschaft für Schwerionenforschung (GSI), Darmstadt, Germany [15], and at the National Institute of Radiological Sciences (NIRS), Chiba, Japan [16]. They have also been applied to proton therapy [17, 18]. However, they are basically limited to 2D imaging, in which the resolution along the axis vertical to the detector faces is insufficient [19]. Therefore, the OpenPET is expected to be the first practical 3D geometry that does not interfere with the beam paths (Fig. 4.2).

4.2 Dual-Ring OpenPET (DROP)

4.2.1 Theory

4.2.1.1 Geometry

The long and continuous FOV including a 360-degree opened gap between two detector rings can be visualized by fully 3D image reconstruction from all the possible lines of response (LORs). Based on the redundant characteristics of 3D PET data, oblique LORs between two separated detector rings are expected to compensate for the missing LORs in the gap, and hence, there is a limited width range in the gap.

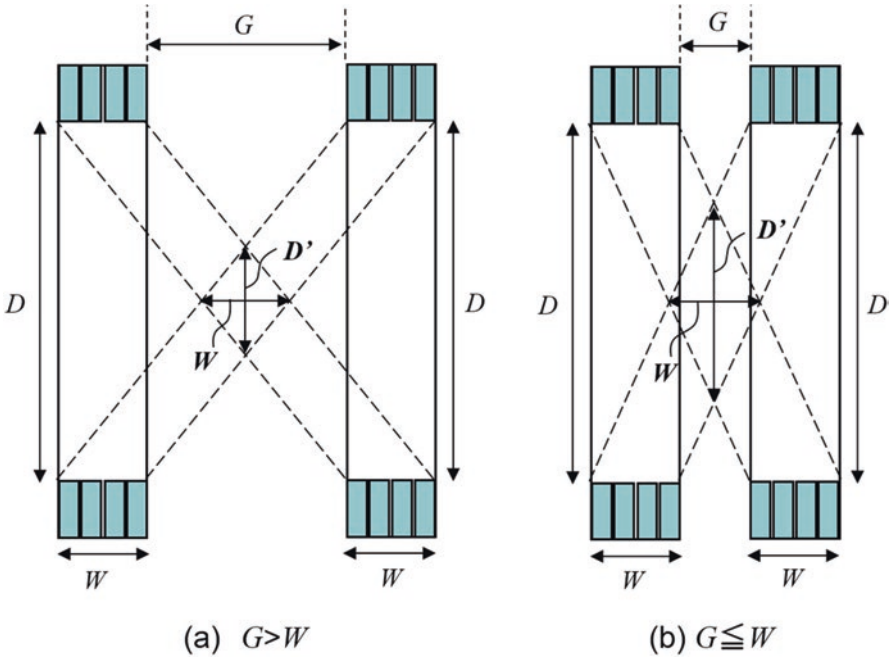

Fig. 4.3 Shows the geometrical analysis of the possible range of the gap G for the DROP geometry of two detector rings of diameter D and axial length W. (**a**) is the case when G is larger than W, and (**b**) is the case $G = W$ or shorter. D' is the minimum diameter of the FOV

Figure 4.3 illustrates a dual-ring OpenPET (DROP) geometry of two detector rings of diameter D and axial length W, separated by a gap G. When $G>W$, the FOV becomes axially discontinuous. In addition, the minimum diameter of the FOV is represented as

$$D' = \frac{DW}{(G+W)}. \tag{4.1}$$

This means that G must satisfy

$$D_0 \le \frac{DW}{(G+W)}, \tag{4.2}$$

when an FOV of more than D_0 in diameter is required. Therefore, in order to obtain the axially continuous FOV of D_0 in diameter, the range of G is limited to

$$G \le \min\left(W, \frac{DW}{D_0} - W\right). \tag{4.3}$$

4.2.1.2 Image Reconstruction

DROP becomes practical with iterative image reconstruction methods since image reconstruction of DROP is an analytically incomplete problem. Therefore, a 3D version of the ordered subset expectation maximization (OS-EM) [20] with a precomputed system matrix was employed. The basic software was originally developed for the jPET-D4 [10]. The system matrix is designed taking into consideration the geometrical arrangement and the radiation penetration of the crystals. Notably, it is possible to compress the system matrix by eliminating zero elements and applying rotational symmetry and an axial shift property of the crystal arrangement precalculation of the system matrix. For the DROP geometries with a variable open space, however, it is not practical to precompute and store a set of system matrixes for each size of open space. Therefore, we proposed a "masked" OS-EM for the DROP geometries with the following conditions:

- The crystals are arranged axially at a regular interval of Δz.
- The gap width, G, is divisible by Δz.
- The detector response functions are only dependent on the ring differences and are axially shift-invariants.

Next, a long gapless scanner having $N = 2N_W + N_{G\max}$ rings was modeled, which completely covers all possible axial FOVs. Here N_w and $N_{G\max}$ are the numbers of crystal rings, which satisfy $W = N_w \Delta z$ and $G_{\max} = N_{G\max} \Delta z$, where $G_{\max}$ is the maximum gap width to be supported. Then we implemented the "masked" OS-EM by applying a mask to the original gapless system, as

$$f_j^{n,m+1} = \frac{f_j^{n,m}}{\sum_l w_l a_{lj}} \sum_{i \in S(m)} w_i a_{ij} \frac{g_i}{\sum_k w_i a_{ik} f_k}, \tag{4.4}$$

where $f_j^{n,m}$ is the j-th image element in the m-th sub-iteration of the n-th iteration. g_i and a_{ij} are the data element and the system matrix element for the N-ring scanner, respectively. $S(m)$ represents a subset of LORs which are used in the m-th sub-iteration. The mask $\{w_i\}$ was defined as

$$w_i = \begin{cases} 0(\text{when the } i-\text{th LOR is missing by the gap}) \\ 1(\text{else}). \end{cases} \tag{4.5}$$

4.2.2 Simulation

4.2.2.1 Scanner

In order to evaluate the imaging performance of the DROP geometries, we simulated a DROP of the two detector rings (D = 827.0 mm, W = 153.6 mm) separated by a variable gap (G ranging from 0 to 2 W) as shown in Fig. 4.4a. The maximum

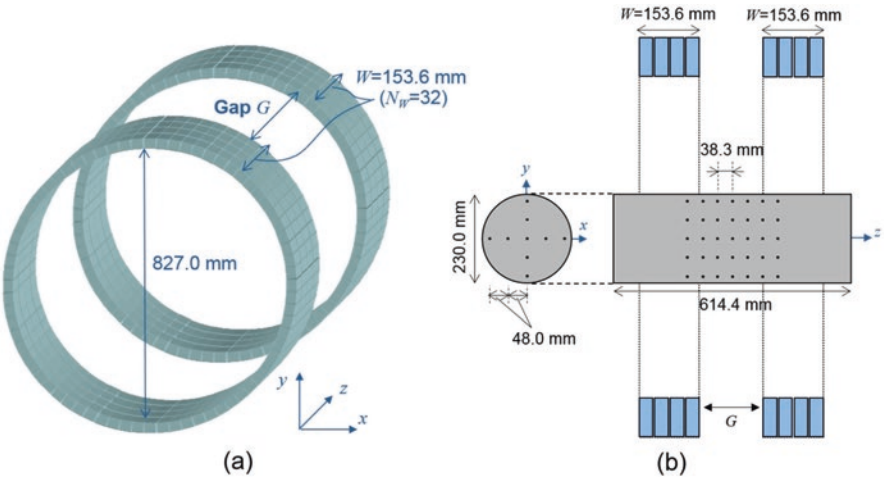

Fig. 4.4 Depicts the simulated DROP scanner (**a**) and the simulated cylinder phantom (**b**). Each detector ring of the DROP has similar dimensions to the HR+ (32 crystal rings, 153.6 mm axial length)

gap size to have an axially continuous FOV is W. However, in order to investigate the image quality when the gap exceeded the limitation, we varied the gap size up to 2 W. Each one of the dual scanners consisted of 4 rings of 72 block detectors. Each block detector consisted of 8 × 8 array of BGO crystals with dimensions of 4.1 mm (transaxial) × 4.4 mm (axial) × 30.0 mm (depth). The axial crystal interval was $\Delta z = 4.8$ mm (center to center), and the number of crystal rings for each one of the dual scanners was $N_W = 32$.

Figure 4.5 shows the minimum diameter of the FOV of the simulated DROP as a function of the gap according to Eq. (4.1). The possible range for the gap to have the axially continuous FOV is also shown according to Eq. (4.3). At the maximum gap for the axially continuous FOV, i.e., $G = W$, the minimum diameter of FOV is decreased to 413.5 mm.

To cover the maximum gap of 307.2 mm, i.e., $N_{G\max} = 64$, the long gapless scanner of $N = 128$ crystal rings was simulated. The voxel size was 2.4 mm^3 and the "mash" factor of two was applied, i.e., two adjacent views were averaged to reduce angular samplings. Then, with the restricted FOV of 268.8 mm in diameter, the dimensions of the projection data became 120 bins × 144 views × 128^2 ring pairs. Projection data were generated by the forward projection using the system matrix. Attenuation and scattering were not included in the simulation.

4.2.2.2 Phantom

In order to demonstrate the imaging performance of the DROP geometry, we simulated a "warm" cylinder of 230.0 mm in diameter and 614.4 mm length, which included 63 "hot" spheres of 4.0 mm diameter (Fig. 4.4b). The warm cylinder was

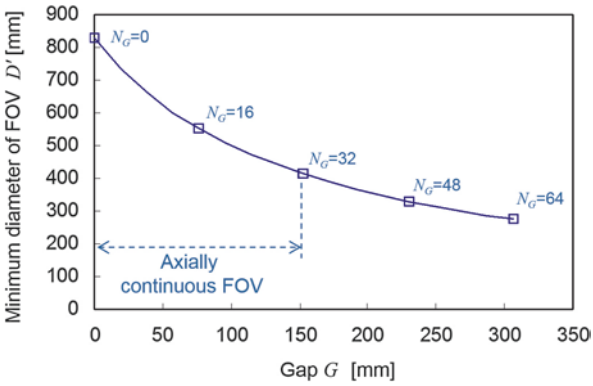

Fig. 4.5 Reveals that the relation between the gap G and the minimum diameter of FOV D' for the simulated DROP. N_G is the number of truncated rings, which satisfies $G = N_G \Delta z$

filled with background activity and the hot spheres contained higher activity. The contrast between background and the hot spheres was 1:5. The mask for the gaps of G = 0.0 mm, 76.8 mm, 153.6 mm, 230.4 mm, and 307.2 mm was applied to the noise-free projection data. The masked 3D OS-EM with 8 subsets and 20 iterations was applied.

4.2.2.3 Results

Reconstructed images are shown in Fig. 4.6. Since the coronal and the sagittal views are identical, only the sagittal views are displayed. In addition, two transaxial slices at the center and at 114.9 mm off-center are shown. The central slices (slice A) of G ranging from 0.0 to 307.2 mm were very similar. The off-center slices (slice B) of G ranging from 0.0 to 153.6 mm were also similar. However, when G>153.6 mm (i.e., the maximum limitation for axially continuous FOV), the blank areas where there is no LOR appeared on both sides of the open space. With the blank areas, distorted point spread functions and low-frequent artifacts were also observed.

The simulation results showed that the DROP visualized a long FOV including the open space. However, it is necessary to minimize the open space according to applications because there is a trade-off relationship between image quality and the size of the open space. In the simulation, artifacts including distorted point spread functions started to appear on both sides of the open space when the gap exceeded 153.6 mm, i.e., the maximum limit for the axially continuous FOV.

4.2.3 Development of a Small Prototype

4.2.3.1 Prototype

We developed a small prototype to show a proof of concept of the OpenPET imaging [21]. The prototype was designed as a compact system (Fig. 4.7) so that it can be easily transported between PET areas and therapy areas such as the Heavy Ion

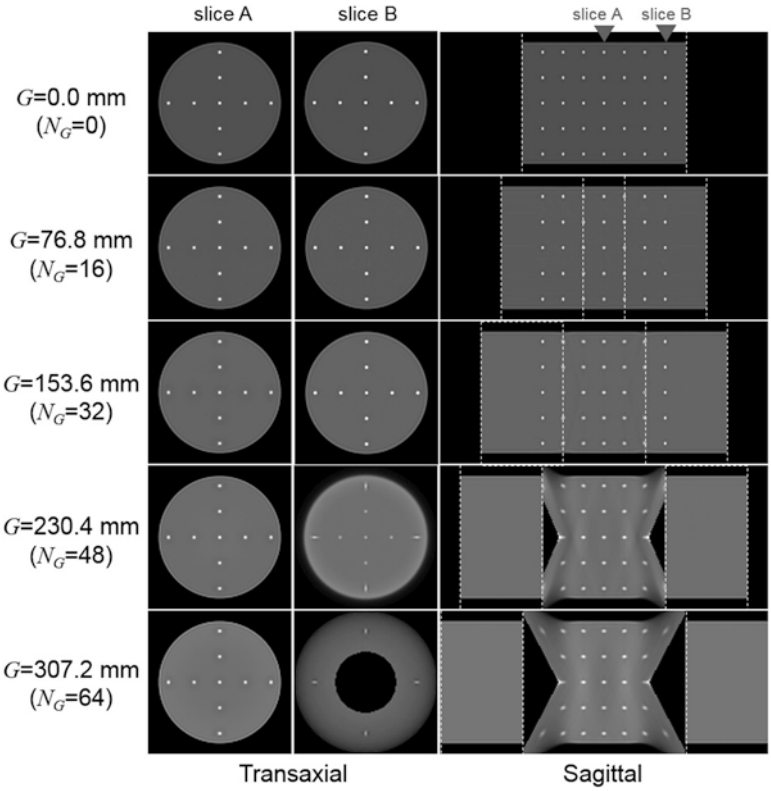

Fig. 4.6 Shows reconstructed images of the simulated warm cylinder phantom with hot spheres for the DROP (*G* ranging from 0.0 to 307.2 mm). In addition to sagittal views, the central slice (slice A) and the off-center slice (slice B) are shown. White dotted lines represent the boundary of the area where detectors are located

Medical Accelerator in Chiba (HIMAC) [22]. Two detector rings of 110 mm diameter composed of 8 block detectors were placed with a variable gap. The height of the center of the detector ring was 125 cm, which equals the height of the HIMAC beam line. Power supply devices and the data acquisition (DAQ) system including positioning and coincidence circuits were placed in the base rack. Details of the DAQ system are available in [23]. In order to reduce radiation damage to electronic circuits caused by secondary particles such as neutrons, front-end circuits such as preamplifiers were separated from photomultiplier tubes (PMTs) and connected by 120 cm long coaxial cables.

Each block detector, which has four-layer DOI capability [11], was composed of a $14 \times 14 \times 4$-layer array of $2.9 \times 2.9 \times 5.0$ mm^3 $Lu_{1.8}Gd_{0.2}SiO_5$:Ce (LGSO) crystals (Hitachi Chemical Co., Japan) and a H8500 PMT. Axial length of the crystal blocks *W* was 42 mm. The gap *G* (i.e., axial length between crystal blocks) was also adjusted to 42 mm, which was the maximum value possible to obtain the axially continuous FOV. The real gap between the two gantry ends of two detector rings

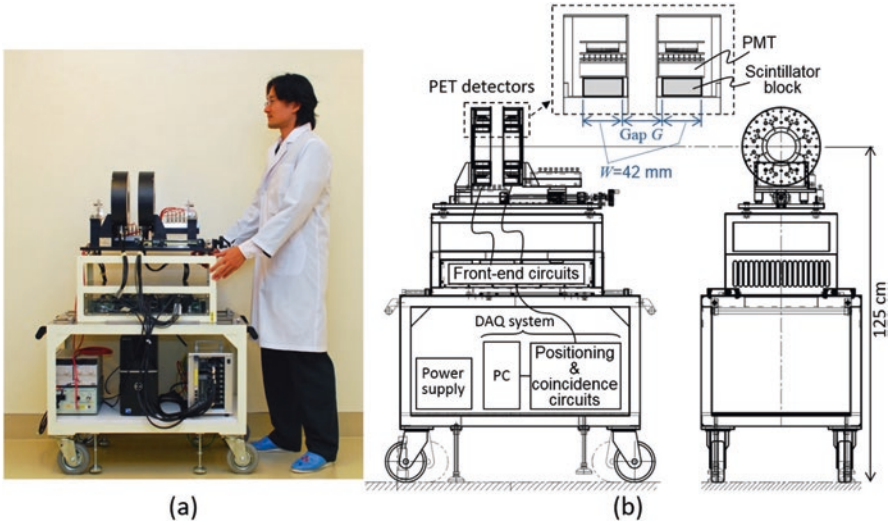

Fig. 4.7 Depicts the small DROP prototype: (**a**) a photograph of prototype and (**b**) sketches showing the positions of the detectors, front-end circuits, data acquisition (DAQ) system, and power supply

was limited to 27 mm by the gantry structure, but the gap will be over 20 cm, which is enough for radiation therapy, if the gantry is extended to the scale of a human body. The energy window was 400–600 keV. At this development stage, we have not completed the timing correction, and the coincidence time window was 60 ns.

As the image reconstruction algorithm, the 3D OS-EM algorithm [20] was applied. Acquired list-mode data were transformed to histogram data before image reconstruction. Random correction was applied by subtracting delayed coincidence, but attenuation correction and scatter correction were not applied. System matrix elements were calculated based on the geometrically defined detector response functions [24]. Iteration parameters were 8 subsets and 10 iterations. The FOV defined in the image reconstruction was 114 mm in diameter and 126 mm in axial length. Two choices of voxel size, $(1.5\ \text{mm})^3$ and $(0.75\ \text{mm})^3$, were applied. The major specifications of the small DROP prototype are listed in Table 4.1.

4.2.3.2 Imaging Performance

Absolute Sensitivity We obtained the absolute sensitivity at the center of the FOV by measuring a 0.047 MBq ^{22}Na point source for 10 min. In order to evaluate loss of sensitivity due to the gap, the absolute sensitivity at the center of the FOV was measured by reducing the gap to the minimum as $G = 42$ mm, 33 mm, 24 mm, and 15 mm. Then the absolute sensitivity for $G = 0$ mm was estimated using an extrapolation (Fig. 4.8). The sensitivity for G = 0 mm is estimated at 8.7% by linearly extrapolating measurement data, while the sensitivity for $G = 42$ mm is 6.6%.

Table 4.1 Major specifications of the developed small DROP prototype

Scanner	
Crystal material	LGSO
Crystal size	$2.9 \times 2.9 \times 7.5$ mm^3
Crystal array	$14 \times 14 \times 4$-layer
PMT	64ch flat panel PMT (Hamamatsu H8500)
Detector arrangement	8 blocks × 2 rings
Ring diameter	110 mm
Gap between crystal blocks (G)	42 mm (minimum 15 mm)
Image reconstruction	
Algorithm	3D OS-EM
Detector response function	Geometrically defined
Voxel size	$(1.5 \text{ mm})^3$ or $(0.75 \text{ mm})^3$

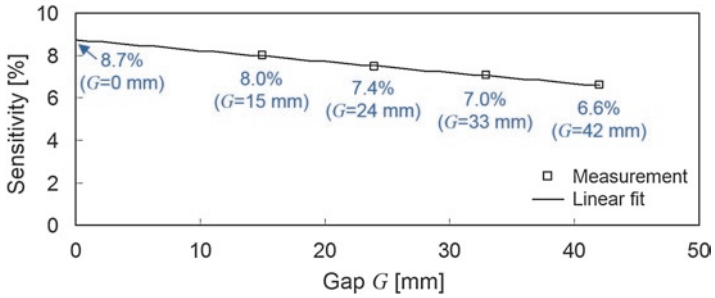

Fig. 4.8 Reveals the absolute sensitivity at the center of the FOV with varying the gap. The sensitivity for $G = 0$ mm was estimated with the linear extrapolation

The results comparing the gap case ($G = 42$ mm) and the non-gap case ($G = 0$ mm) clearly show what we have sacrificed for the open geometry: about 24% of the sensitivity is lost due to the solid angle effect.

Phantom Imaging For demonstration, we measured a small rod phantom, which had a similar structure to a micro-Derenzo phantom (Fig. 4.9). The phantom consisted of an outer hollow cylinder and an inner solid cylinder of 36.1 mm diameter and 17.8 mm length. The inner solid cylinder contained rods of various diameters (1.0 mm, 1.6 mm, 2.2 mm, 3.0 mm, 4.0 mm, and 4.8 mm). First, the phantom was placed vertically with the rods parallel to the axial direction ("vertical" position), and then, it was placed horizontally ("horizontal" position). In addition, the phantom was placed in two positions: in-ring and in the gap. The phantom (filled with 1.3 MBq ^{18}F solution) was measured in the order of in-ring vertical, gap vertical, in-ring horizontal, and gap horizontal. Scan times, which were adjusted to correct for radioactive decay, were 20 min, 23 min, 28 min, and 34 min, respectively. With the random rate varying from 15 to 6%, the measured prompt coincidence counts were 14.1 M, 29.7 M, 21.2 M, and 28.3 M, respectively. The 0.75 mm voxel was used in image reconstruction. The comparison of transaxial slices obtained in-ring

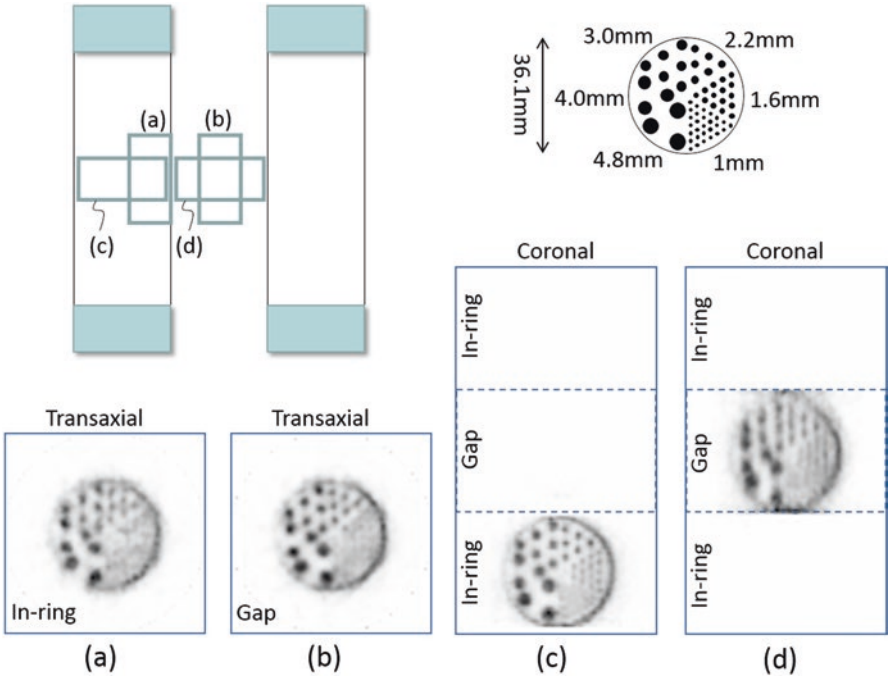

Fig. 4.9 Shows the reconstructed images (0.75 mm voxel) of the small rod phantom at four different positions (**a**–**d**)

(Fig. 4.9a) and in the gap (Fig. 4.9b) supports the feasibility of the OpenPET imaging since almost the same image is obtained even in the gap. The image in the gap seems to be rather superior to that in the ring, because sensitivity in the gap is about twice as high as that in the ring. Rods of 2.2 mm diameter are completely separated. On the other hand, the effect of the loss of axial spatial resolution is seen in the comparison of coronal slices obtained in-ring (Fig. 4.9c) and in the gap (Fig. 4.9d), although the rods are still separated in the gap.

4.2.3.3 Small Animal Imaging

Colon-26 cancer cells (1.0×10^6) were inoculated subcutaneously into both flanks of a female BALB/c-nu/nu mouse (16.5 g weight, Japan SLC Inc., Japan). After 10 days, the mouse was fasted overnight before PET scanning. Then 1.6 MBq ^{18}F-labeled fludeoxyglucose (FDG) was injected intravenously via a tail vein. After 70 min, the animal was sacrificed and placed so that the tumors were located in the gap. Then 10.3 M prompt coincidence counts and 0.6 M delayed coincidence counts were measured for a 10 min PET scan. The 0.75 mm voxel was used in image reconstruction. A reconstructed image is shown in Fig. 4.10. The tumors located in the

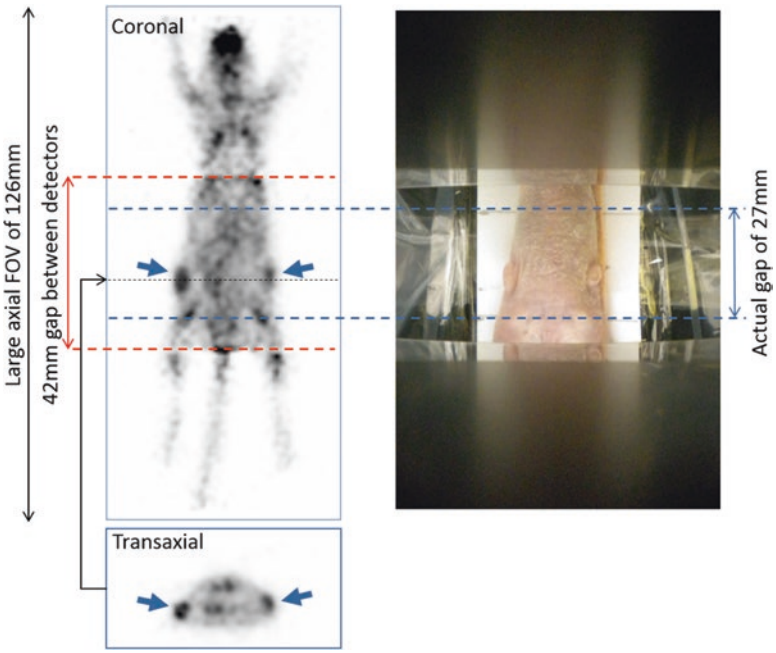

Fig. 4.10 Shows the results of small animal imaging. A reconstructed image (0.75 mm voxel) of the tumor inoculated mouse using ^{18}F-FDG. The figure reveals coronal and transaxial slices crossing two tumors (indicated by the *arrows*)

gap are clearly visualized. This result also shows the effect of the extension of the axial FOV. An axial FOV of 126 mm is obtained with the detectors that originally cover only an 84 mm axial FOV.

4.2.4 In-Beam Imaging of Carbon Ion Beam

For a proof of concept of PET imaging during radiation therapy, our group carried out in-beam experiments in the HIMAC to visualize in situ particle distribution in a phantom. In a usual carbon (^{12}C) beam irradiation, it has been reported that the activity of positron emitters, produced by fragmentation reactions, is generally low in addition to the theoretical difference between the dose distribution and positron emitter distribution [14]. Therefore, instead of the ^{12}C beam, we used a ^{11}C radioactive (RI) particle beam as an incident beam, directly [25] in the secondary beam port. This beam port is where various RI beams can be generated as secondary beams from the ^{12}C beam by irradiating a Be target. Because the projectiles themselves are positron emitters, we expected to obtain PET images directly corresponding to the distribution of primary particles.

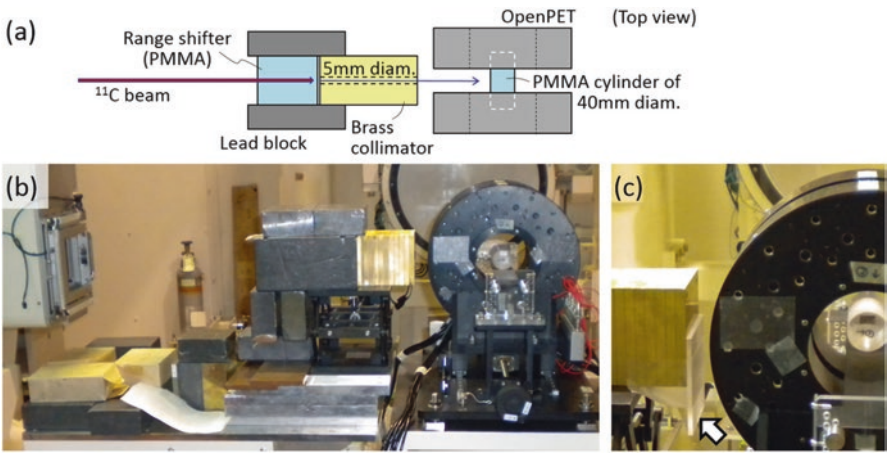

Fig. 4.11 Shows the experimental setup for in-beam imaging tests of the developed small DROP prototype, installed in the HIMAC. (**a**) is a schematic top view illustration showing details of the photograph in (**b**). Insertion of an additional 5 mm thick PMMA board (**c**) is indicated by the *arrow*, which covers bottom half the collimated beam

4.2.4.1 Experiment Setup

Figure 4.11 shows the experimental setup. The small DROP prototype was positioned so that the beam passed through the gap. A polymethyl methacrylate (PMMA) cylindrical phantom (40 mm diameter, 100 mm length) was placed in the center of the FOV and irradiated along the radial direction by a ^{11}C pencil beam. The beam intensity was about 5×10^6 particles per second (pps), which was the maximum possible in the secondary beam port, and the beam energy was 332.6 MeV/u. Therefore, a PMMA range shifter of appropriate thickness (150 mm) was used to stop the beams near the center of the phantom. After passing beams through the brass collimator (5 mm diameter, 150 mm length), the beam intensity was limited to 1.7×10^5 pps. It has been reported that PET data, which are measured at the moment of irradiation, include increased random coincidences by prompt gamma rays [26, 27]. On the other hand, the irradiation in the HIMAC has a 3.3 s cycle, in which the particles are delivered as a "bunch" of about 1.8 s duration followed by about 1.5 s pause. Hence, for the in-beam PET measurements, we extracted a useful list-mode data for each irradiation and synchronized it with this bunch cycle.

As a demonstration of the range resolution performance, an additional PMMA board of 5 mm thickness was used to cover half of the collimated beam, as shown in Fig. 4.11c. The phantom was irradiated by the ^{11}C beam for 20 min and in-beam PET data were measured during irradiation. The voxel size in image reconstruction was also 1.5 mm.

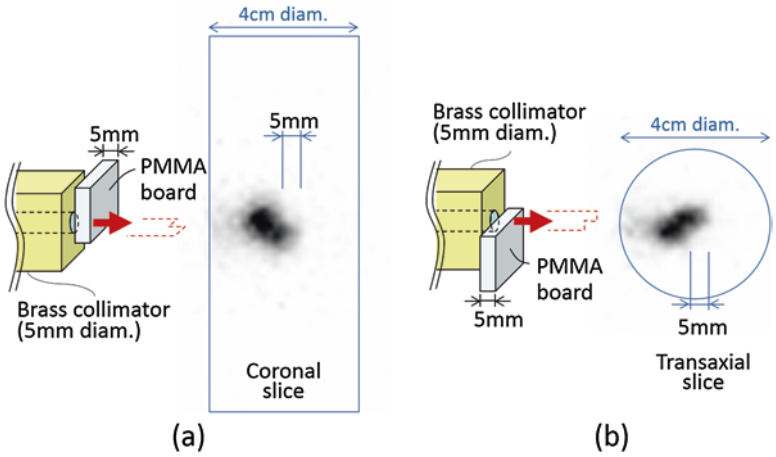

Fig. 4.12 Presents a schema of the resolution performance for a 5 mm difference in range. (**a**) represents reconstructed images (1.5 mm voxel) from in-beam PET data during 20 min ^{11}C irradiation with the PMMA board of 5 mm thickness covering the right half, while (**b**) is the bottom half of the collimated beam

4.2.4.2 Results

Reconstructed images from in-beam PET data during the 20 min ^{11}C irradiation are shown in Fig. 4.12. The 5 mm difference in the range was clearly visualized both in the coronal slice and the transaxial slice, which supports our conclusion that at least a 5 mm resolution in range could be detected three-dimensionally, with in-beam measurement by the DROP with ^{11}C irradiation.

4.2.5 Real-Time Imaging for Tumor Tracking

An image reconstruction calculation usually requires a time period in the order of minutes, but there are big demands in real-time imaging for OpenPET. For example, real-time PET-guided medical procedures such as radiation therapies and biopsies are feasible by visualizing and tracking a target tumor, which is labeled with radioactive tracer in addition to the in-beam imaging. It should be noted that tumor tracking is a much more challenging application in terms of the real-time requirement. Real-time tracking is desirable, especially for mobile organs such as the lungs, which move with respiration. In contrast to conventional tumor tracking methods, which use implantation of surrogates, the real-time OpenPET imaging enables the direct visualization of the tumor. Real-time imaging of PET is a challenging task because of its computational burden in image reconstruction. Conventionally, PET images are reconstructed after all data are acquired. The time to display an image takes at least several minutes. Thus, in order to perform

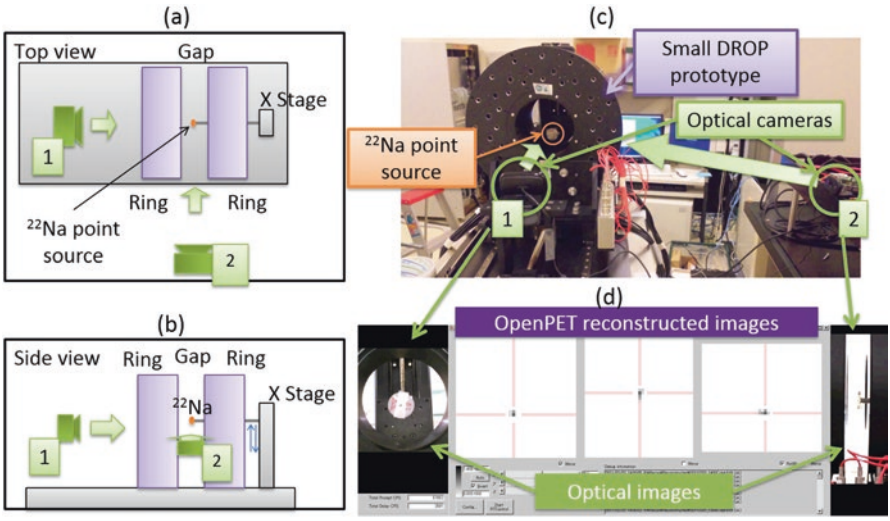

Fig. 4.13 Depicts the tracking ability demonstration setup: (**a**) is the schematic illustration of the top view; (**b**) reveals the side view; (**c**) shows a photograph of the demonstration setup; and (**d**) provides example images captured during the tracking demonstration. ^{22}Na point source (1 MBq) was set between the ring gap and moved up and down with a 30 s cycle

real-time imaging, a cycle of data acquisition, data transfer, image reconstruction, and display needs to be completed within less than 1 second. For the real-time image reconstruction, we implemented the 3D one-pass list-mode dynamic row-action maximum likelihood algorithm (DRAMA) [28, 29] on a graphics processing unit (GPU). In addition, a data transfer control system was implemented, so that the reconstruction speed is stabilized by limiting the number of list-mode events processed at one time [30].

4.2.5.1 Experimental Setup

We demonstrated the system performance in terms of the real-time tracking ability by a point source tracking experiment. Figure 4.13 shows the experimental setup and an image frame captured during the demonstration. In the demonstration, a ^{22}Na point source (1 MBq) was put on a moving stage with a long bar so that the source was placed between the gaps of the small DROP prototype. The number of counts to be used in the GPU-implemented 3D list-mode DRAMA was limited below 5000, and voxel size was set to $3.0 \times 3.0 \times 3.0$ mm^3 for better frame rate performance. The reconstructed image size was $38 \times 38 \times 42$ voxels.

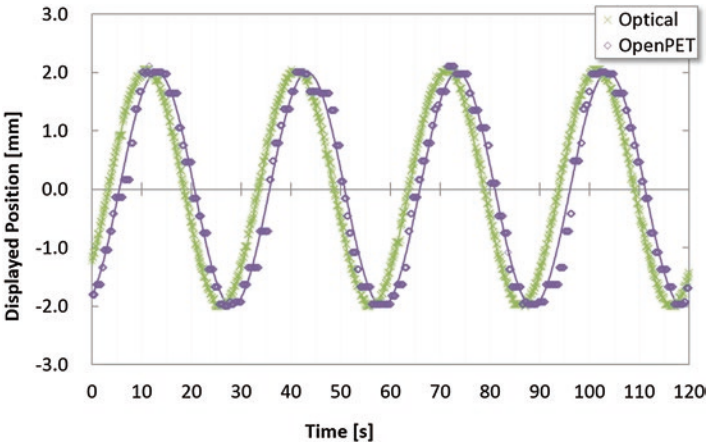

Fig. 4.14 Highlights displayed positions of the point source in the images obtained by the optical camera and by the OpenPET during the tracking demonstration. From the sine curve fitting, the delay was determined as 2.1 s

4.2.5.2 Results

In the demonstration, transaxial, coronal, and sagittal slices of the reconstructed OpenPET images and movies of a moving point source captured by optical cameras were simultaneously displayed on the PC screen (Fig. 4.13d). The point source moved up and down with a 30 s cycle sine curve, and the real-time viewer showed the reconstructed images with a frame rate of 2 frames per second (fps). Figure 4.14 shows the displayed point source position on the screen. From the sine curve fitting, an average delay time of 2.1 s was obtained and the mean error was 2.0 mm. The time-delay correction method using a supporting sensor was also developed in order to compensate for the delay [31].

4.3 Single-Ring OpenPET (SROP)

For the purposes of in-beam PET and tumor tracking, the FOV that we need to image appears only in the gap area between the two detector rings. It is not necessary to image the FOV in the detector ring area for these applications. Therefore, our group proposed a second-generation OpenPET geometry, single-ring OpenPET (SROP), as a more efficient geometry [32]. The SROP can provide an accessible and observable open space with higher sensitivity and a reduced number of detectors compared to the previous generation geometries. Figure 4.15a shows a conceptual illustration of the SROP comparing with the first-generation OpenPET; 4.15b depicts DROP, and 4.15c displays an in-beam geometry, in which the conventional PET is positioned at a slant angle relative to the bed to form an accessible space

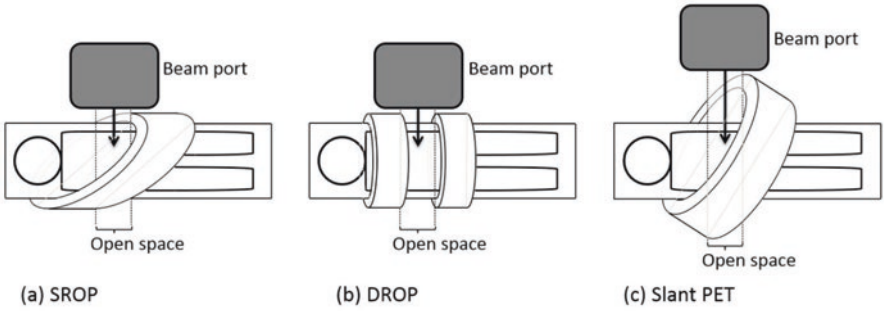

Fig. 4.15 Shows a conceptual illustrations of PET geometries with an accessible open space to the patient: (**a**) reveals that the SROP has the shape of a cylinder cut at a slant angle; (**b**) that the beam port can be placed near the patient bed, the same as in DROP; and (**c**) that conventional cylinder PET can also provide an open space by placing it at a slant angle relative to the patient bed

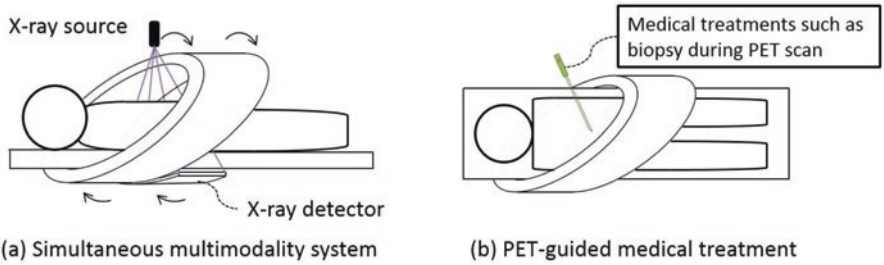

Fig. 4.16 Presents the applications of the SROP: (**a**) as a simultaneous PET-CT multimodality system and (**b**) as a as a PET-guided biopsy and medical treatment

(hereinafter referred to as "slant PET"). Compared with the slant PET, the single-ring OpenPET is expected to provide higher sensitivity with a smaller number of detectors. Thus, in the case of in-beam PET, it provides a closer positioning of the beam port, which minimizes beam broadening. Other possible applications of the SROP are shown in Fig. 4.16.

4.3.1 Theory

The sensitivity of PET is highly correlated with solid angle coverage where the coincidence detection is possible; the solid angle coverage is hereinafter referred to as geometrical sensitivity. On the other hand, the detector surface area is correlated with the number of detectors used for constructing the actual system. Figure 4.17 illustrates geometries of SROP, DROP, and slant PET. The open space with the size of C is achieved with the patient bed width of B and the detector ring width of W.

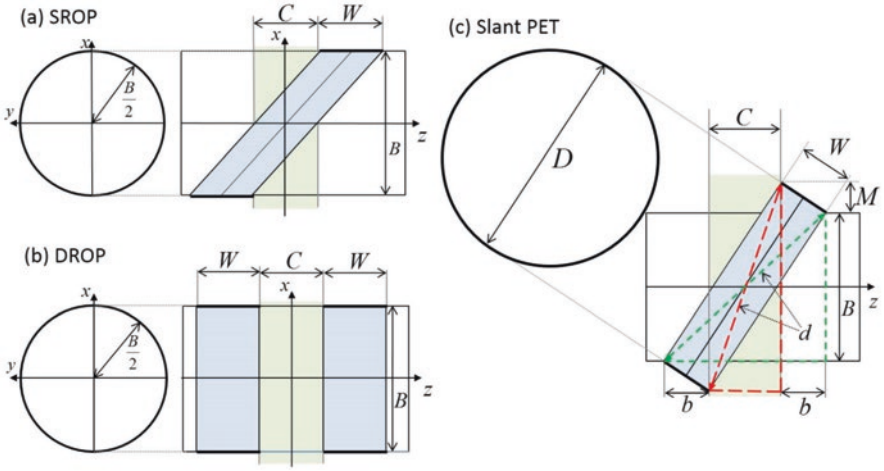

Fig. 4.17 Depicts the geometrical analysis of the SROP (**a**), DROP (**b**), and slant PET (**c**). The widths of the open space, detector ring, and patient bed are notated as *C*, *W*, and *B*, respectively

The geometrical sensitivity *R* and the detector surface area *S* for each geometry are calculated as follows:

SROP

$$R_{\mathrm{SROP}} = \frac{1}{4\pi}\int_0^{2\pi}\left\{\frac{(W+C)\sin\phi + W}{\sqrt{\{(W+C)\sin\phi + W\}^2 + B^2}} - \frac{(W+C)\sin\phi - W}{\sqrt{\{(W+C)\sin\phi - W\}^2 + B^2}}\right\}d\phi, \tag{4.6}$$

$$S_{\mathrm{SROP}} = \pi WB. \tag{4.7}$$

DROP

$$R_{\mathrm{DROP}} = \frac{2W+C}{\sqrt{(2W+C)^2 + B^2}} - \frac{C}{\sqrt{C^2 + B^2}}, \tag{4.8}$$

$$S_{\mathrm{DROP}} = 2\pi WB. \tag{4.9}$$

Slant PET (SP)

$$R_{SP} = \sin\left(\arctan\frac{W}{\sqrt{d^2 - W^2}}\right), \tag{4.10}$$

$$S_{SP} = \pi W\sqrt{d^2 - W^2}, \tag{4.11}$$

where d is determined by solving the following system of equations:

$$\begin{cases} d = \sqrt{(C+2b)^2 + B^2} \\ d = \sqrt{C^2 + \left(B + 2\sqrt{W^2 - b^2}\right)^2} \end{cases}. \tag{4.12}$$

We note that an additional margin is required to place the beam port in the slant PET case. The margin M is calculated using the following equation:

$$M = \sqrt{W^2 - b^2}, \tag{4.13}$$

where b is determined by solving Eq. (4.12).

Figure 4.18 shows the geometrical sensitivity at the center plotted against the detector surface area. As fixed parameters, the bed width of $B = 600$ mm and open gap of $C = 300$ mm were selected to provide a sufficient open space during ion beam therapy. The number of block detectors is defined as the surface area of each geometry divided by the area of one block detector, which is also shown above the graph to give an intuitive insight. Here, we assumed that the area of the block detector was 2500 mm^2 (i.e., 50 mm × 50 mm). When the detector surface area was 500,000 mm^2, in which the equivalent number of block detectors was 200, the geometrical sensitivities of the SROP, DROP, and slant PET were 27.8%, 23.9%, and 22.1%, respectively.

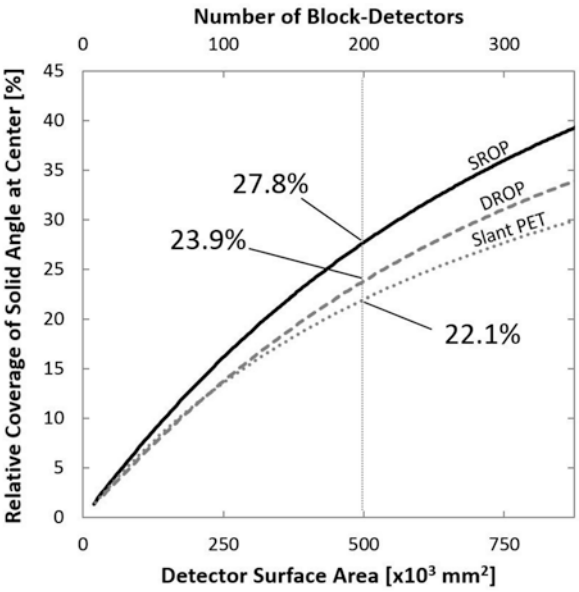

Fig. 4.18 Shows the geometrical sensitivity at the center against the number of block detectors for the open gap length C = 300 mm and bed size B = 600 mm. When the detector surface area was 500,000 mm^2, in which the equivalent number of block detectors was 200, the geometrical sensitivities of the SROP, DROP, and slant PET were 27.8%, 23.9%, and 22.1%, respectively

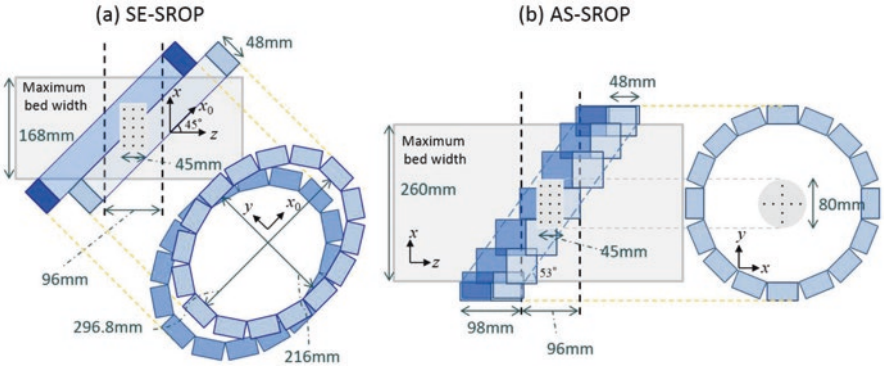

Fig. 4.19 Presents simulation geometries of the small SE-SROP (**a**) and AS-SROP (**b**), with illustrations of the simulated cylinder phantom including the point-like sources

4.3.2 Simulation

In contrast to the DROP, the SROP has a FOV focused at the open space. Therefore, the SROP can provide a wider open space and higher sensitivity at the center of the FOV with the same number of detectors. However, realization of the SROP with rectangular block detectors remains a challenging problem because the cut ends of the detector ring are elliptic. So far, we have considered two candidates for the detector arrangement method to realize the SROP. The first method is a slant-ellipsoid type of SROP (SE-SROP), in which the ellipse-shaped detector rings are stacked at a slanted angle (Fig. 4.19a) [33]. The second method is an axial-shift type SROP (AS-SROP), in which the block detectors originally forming a conventional cylindrical PET scanner are axially shifted little by little so that the center of each detector surface, positioned on the parallel planes, is slanted against axial direction (Fig. 4.19b) [34]. We conducted a numerical simulation study to compare these two methods for constructing the small SROP with respect to their imaging performance and the effect of utilizing DOI detectors. For this simulation, each block detector was composed of a four-layer 16 × 16 array of 3.0 × 3.0 × 7.5 mm^3 Gd_2SiO_5 (GSO) scintillators. In the non-DOI cases, each block detector was composed of a 16 × 16 array of 3.0 × 3.0 × 30.0 mm^3 GSO scintillators. The small SROP was designed with two detector rings of 16 block detectors. For both types, an open space with the width of 96.0 mm was obtained. A cylinder phantom including point-like sources was simulated. The diameter of the point-like sources was 4.0 mm, and the contrast ratio of the radioactivity in the point-like sources and the background cylinder was 10:1. Projection data were generated by forward projection using a geometrically defined system matrix based on the sub-LOR model [25]. Noise, attenuation, and scattering were not included in the simulation. Images were reconstructed by the 3D OS-EM method with 8 subsets and 10 iterations. The voxel size was 1.5 × 1.5 × 1.5 mm^3, which was half of the scintillator size.

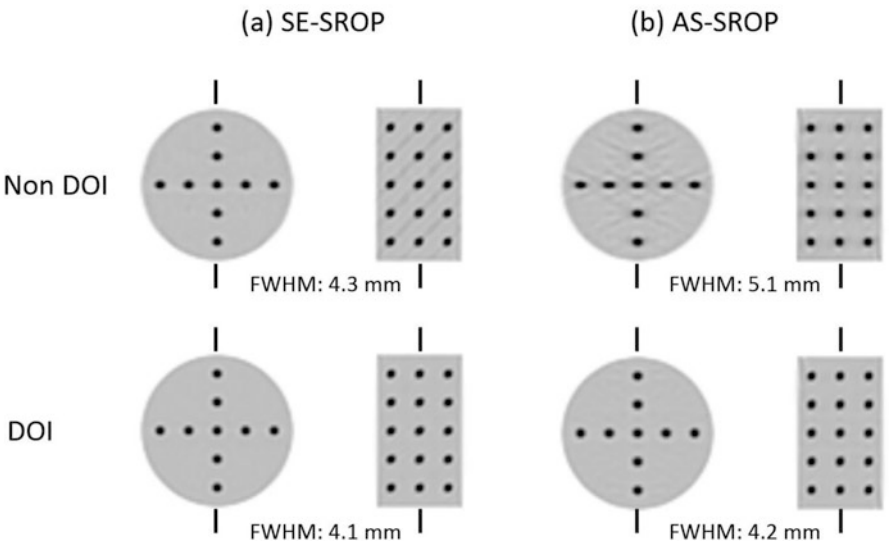

Fig. 4.20 Shows the reconstructed images in the simulation of the small SE-SROP (**a**) and AS-SROP (**b**) types. The top row is without DOI measurement and the bottom row is with the DOI measurement. For each pair of images, the left is the transaxial slice and the right is the coronal slice. The average FWHMs are shown

Figure 4.20 shows the reconstructed images for the simulation of the small SE-SROP and small AS-SROP with and without DOI measurements. In the case of no DOI simulation, artifacts appeared in the coronal slice of the reconstructed image for the SE-SROP and in the transaxial slice of that for the AS-SROP. In the case of DOI simulation, no visible artifacts appeared in both types. The full width at half maximum (FWHM) was calculated by averaging for transaxial and axial FWHMs of all point sources to evaluate spatial resolution. As a result, we found the DOI detector improved the spatial resolution in both cases. Therefore, we concluded that both types had almost the same imaging performance of an acceptable quality using DOI detectors.

4.3.3 Development of a Small Prototype

Figure 4.21 shows the design illustrations of the small AS-SROP prototype [34] that had two modes (open and closed), which are shown in Fig. 4.22. The open mode formed the SROP geometry and the closed mode formed the cylindrical PET geometry. Sixteen detector units each of which consisted of two DOI detectors were arranged to form a perfect circle with a diameter of 250 mm. Detector units had an axial shift mechanism so that they could be transformed into the SROP having an open space of 139 mm. In the open mode, the center of each detector surface,

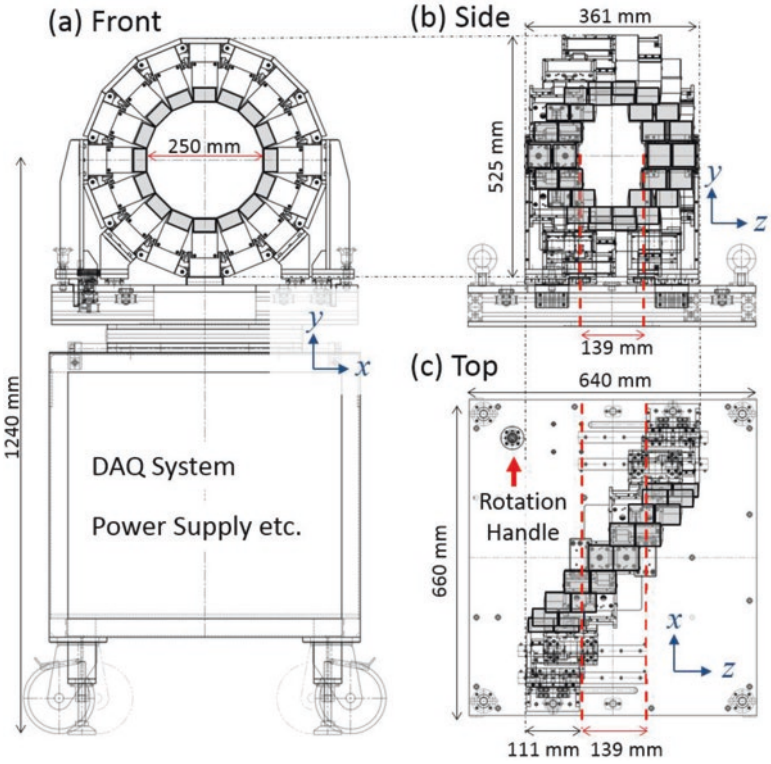

Fig. 4.21 Shows design illustrations of the small AS-SROP prototype: (**a**) depicts the front, (**b**) the side, and (**c**) the top views. *Dark boxes* indicate scintillator blocks

positioned on the parallel planes, was slanted 45° against the axial direction. For shifting purposes, each detector unit was connected to the neighboring detector units by linear guides. Transformation between the cylindrical PET (Fig. 4.22a) and the SROP (Fig. 4.22b), which was controlled by one rotation handle, was completed within 10 s.

Each DOI detector consisted of a H8500 PMT and the four-layer 16 × 16 array of Zr-doped GSO (GSOZ) scintillators (Hitachi Chemical Co., Japan) with a size of $2.8 \times 2.8 \times 7.5$ mm^3. We should note that while the lutetium (Lu)-based scintillators are widely used for PET, Lu has intrinsic radioactivity. Therefore, we used Lu-free scintillators to reduce the background activity as low as possible for low activity measurements. The output signals of two DOI detectors stacked axially were projected onto one 2D position histogram by an Anger calculation. Each DOI detector was in coincidence except for the neighboring DOI detectors. Coincidence data were corrected as list-mode data. The random correction was done by delayed coincidence data subtraction. The energy window was 400–600 keV and the timing window was 20 ns.

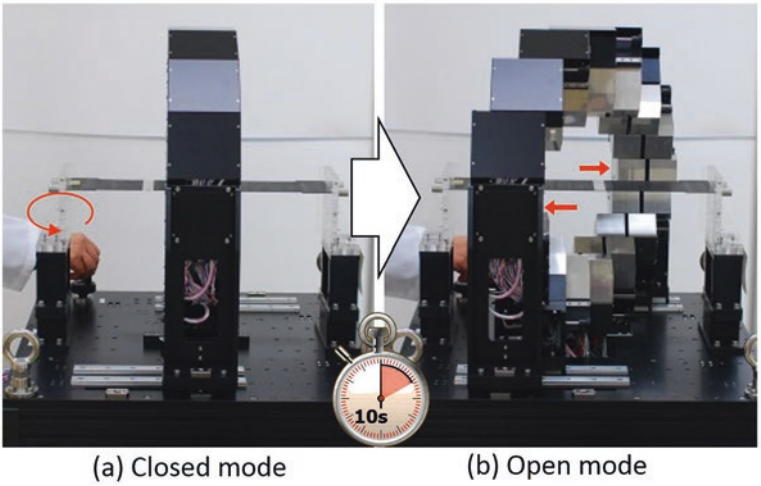

Fig. 4.22 Provides photographs of the small AS-SROP prototype taken from the side in the closed conventional PET (**a**) and OpenPET (**b**) modes. The transformation from the closed mode to the open mode was completed within 10 s

The compact and all-in-one design of the prototype allowed us to use it for in-beam experiments in the HIMAC. The gantry stage had wheels, all the electronics, data acquisition (DAQ) system, and power supply stored in the gantry stage (Fig. 4.21a). Therefore, the entire system could be easily transported between PET areas and the irradiation room in the HIMAC.

We evaluated the basic performance of the prototype. The spatial resolution and sensitivity were 2.6 mm and 5.1% for the open mode and 2.1 mm and 7.3% for the closed mode. The AS-SROP enables in-beam PET imaging at a slight cost of imaging performance. The decrease of the performance can be minimized, for example, by transforming into the close mode immediately after the irradiation while maintaining the open space only for the in-beam PET measurement.

For an imaging demonstration, a small rod phantom, which had a similar structure to the micro-Derenzo phantom, was measured. The rod phantom consisted of an outer hollow cylinder and an inner solid cylinder with a diameter of 36.1 mm and a length of 17.8 mm. The phantom was filled with ^{18}F solution with total activity of 2.5 MBq, and it was measured at the center of the FOV with both modes. We measured two positioning angles of the phantom, standup and laydown, so that the inner rod holes were directed in the z direction and y direction, respectively. Measurement time was controlled so that the total number of decays became almost the same for each measurement. Because the number of coincidence events was large, the list-mode data were converted to the LOR histogram. Images were reconstructed by the 3D OS-EM algorithm with 8 subsets and 10 iterations. The random correction was applied by subtracting delayed coincidence but attenuation correction and scatter correction were not applied. The voxel size was $1.5 \times 1.5 \times 1.5$ mm^3.

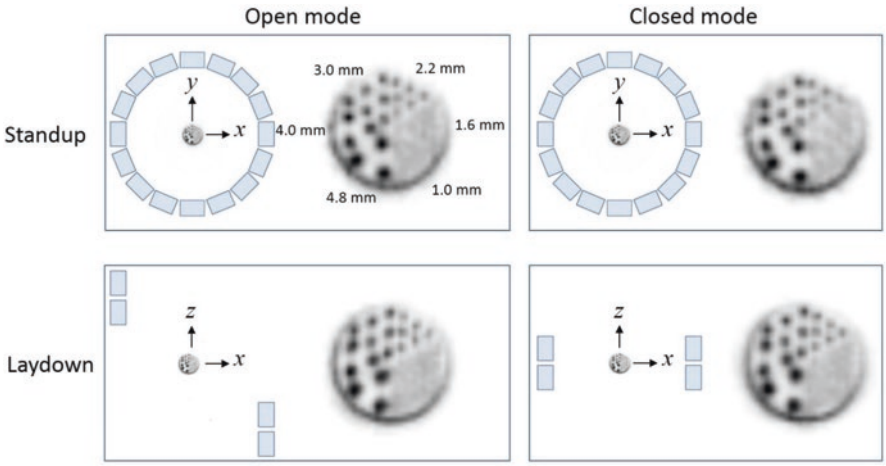

Fig. 4.23 Reveals reconstructed images of the small rod phantom

Figure 4.23 shows reconstructed images of the small rod phantom for the open mode and the closed mode using the 3D OS-EM with 8 subsets and 10 iterations. Center slices perpendicular to the rod directions are shown. The measured numbers of counts were 189 M (standup) and 181 M (laydown) for the closed mode and 132 M (standup) and 129 M (laydown) for the open mode. Rods of 2.2 mm diameter were clearly separated for both modes and both positioning angles of the phantom.

4.3.4 In-Beam Imaging of Carbon Ion Beam

The small prototype was brought into the HIMAC irradiation room where we conducted the in-beam imaging tests. A PMMA phantom was irradiated with an RI beam of ^{11}C, which has a half-life of about 20 min. The RI beam was generated as a secondary beam from the ^{12}C irradiation onto a Be target. Figure 4.24 shows the experimental setup. The dimensions of the rectangular cuboid PMMA phantom were $40 \times 40 \times 100$ mm^3, and an additional PMMA board with a thickness of 9 mm was used to cover the upper half of the beam. The irradiation time was about 10 s and a dose of about 2.5 Gy was given. The beam intensity was about 5×10^6 particles per second and the beam energy was about 340 MeV/u. Therefore, the Bragg peak position in PMMA was at about 168 mm. A PMMA range shifter of 115 mm thickness was used so that the Bragg peak position was moved to 53 mm from the entrance of the phantom. PET data were measured during the irradiation and for 20 min after the irradiation ended. Because the irradiation beam in the HIMAC had a cycle of 3.3 s with beam-on time (spill on) of about 1.8 s and a beam-off time (spill off) of about 1.5 s, PET data for the spill-off time were extracted. Because the number of counts acquired for the in-beam measurement was small, the 3D list-mode maximum likelihood expectation maximization (LM-MLEM) was employed for the PET image reconstruction. The number of iterations was 50 and the voxel size was

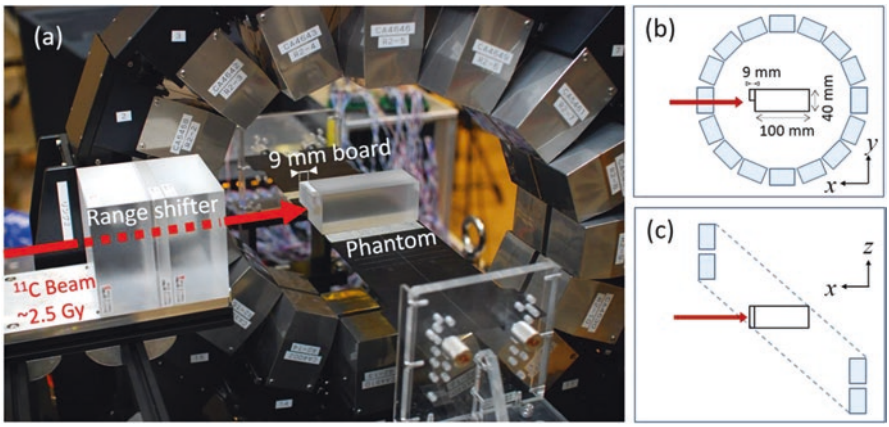

Fig. 4.24 Depicts the setup for PMMA phantom irradiation by the ^{11}C beam and in-beam PET measurements. A photograph of the setup (**a**) and illustrations for front (**b**) and top (**c**) views are shown

1.5 × 1.5 × 1.5 mm^3. Random correction and attenuation correction were applied, but scatter correction was not applied because the phantom size was small enough so that the scatter effects can be ignored.

Figure 4.25 shows the in-beam measurement results for the ^{11}C beam irradiation. The count rates for coincidence events were recorded. The phantom was irradiated with spills (3.3 s irradiation cycle) to give the total dose of about 2.5 Gy. The count rate graph shows that there were huge numbers of counts during the spill-on time, due to the prompt γ-rays. However, they were single γ-rays and could not be used for PET imaging. Even if there were counts from positron emitters, it was hard to distinguish them from background single γ-rays. On the other hand, coincidence events in the spill-off time, when the prompt γ-rays were not detected, could be used for imaging. Figure 4.25b, c shows images reconstructed from counts measured between spills and for 20 min after the irradiation. The number of counts was 626 k counts. Figure 4.25d shows the profiles of single voxel lines along the beam direction for the upper part with the 9 mm PMMA board and for the lower part without it. The peak position of the lower part was calculated by parabola fitting as 55.0 mm (planned Bragg peak at 53 mm). The difference in peak positions was clearly observed and measured as 8.8 mm.

4.4 Development of a Full-Size DROP System

4.4.1 System Development

The full-size DROP prototype consists of two detector rings, and each detector ring has two subrings of 40 detectors (Fig. 4.26). Each detector consists of 16 × 16 × 4 array of GSOZ (2.8 × 2.8 × 7.5 mm^3). The portable gantry has a compact design;

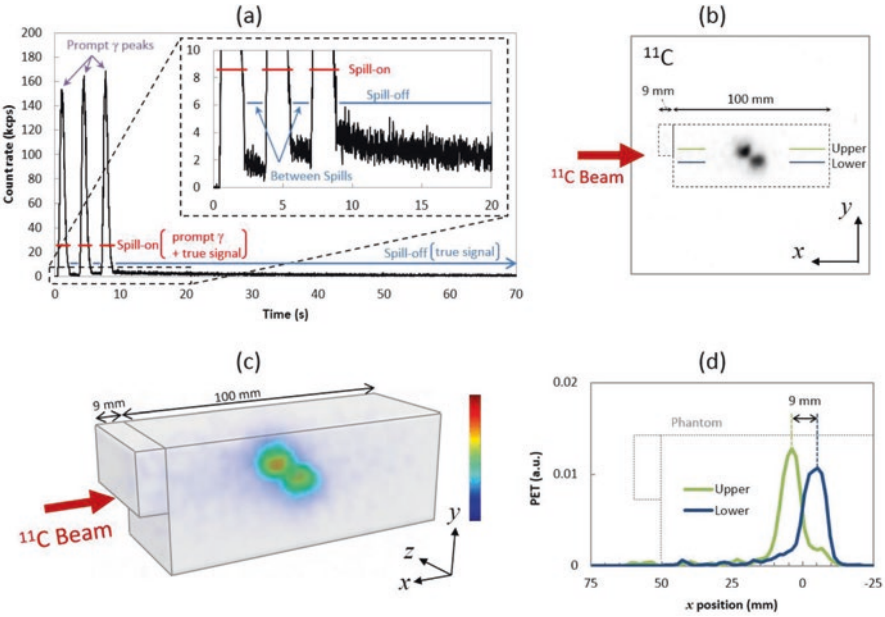

Fig. 4.25 Shows the results of the in-beam experiment, which demonstrates the results for imaging the 9 mm difference given by the Bragg peak positions: (**a**) reveals count rates in the first 70 s of the in-beam measurement of the ^{11}C beam, (**b**) is the center slice of the image reconstructed from counts measured between spills and for 20 min after the irradiation, and (**c**) is the 3D visualization of the image with the shape of the PMMA phantom, indicated by dotted lines and gray rectangular parallelepipeds. Profiles along the beam direction for upper and lower lines indicated in (**b**) are plotted in (**d**), in which the center of the FOV is $x = 0$

each detector ring has a 940 mm outer diameter and 171 mm axial length for the detector inner bore of 640 mm diameter and 113 mm axial length.

The key technology, which enabled OpenPET, is the four-layered DOI detector. In order to measure radiations from the limited activity produced though fragmentation reactions, GSOZ was chosen for the scintillators instead of Lu-based scintillators because GSOZ contains less natural radioactivity, although timing performance was compromised. On the other hand and in order to compensate for the limited light yield, we used 64channel flat-panel PMTs with a super-bi-alkali photocathode (Hamamatsu R10552–100-M64), which had a 30% higher quantum efficiency [35]. Then, to enable stable in-beam PET measurement even under high background radiations, voltage divider circuits were designed so as to have five times higher linearity.

Lastly to avoid severe radiation damage to ASICs, gain control circuits were not implemented in the front-end circuits, while position analyzer circuits were placed with a 15-m cable extension. A data acquisition system was developed based on the single events collection.

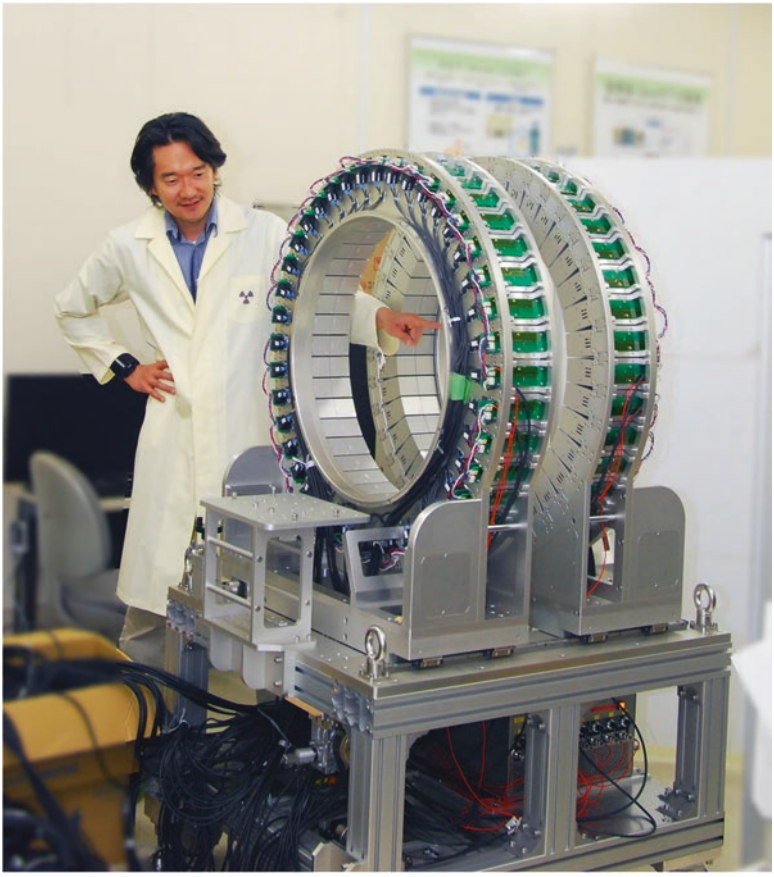

Fig. 4.26 Developed full-size DROP

4.4.2 Imaging Test

The system was tested with a carbon ion beam of clinical intensity at HIMAC as shown in Fig. 4.27. Phantom images were obtained by applying a GPGPU-based list-mode iterative reconstruction algorithm with geometrical detector response modeling. A PMMA phantom ($10 \times 10 \times 30$ cm^3) was irradiated by a ^{12}C ion beam (mono energy pencil beam). About 2.5 Gy was given during about 10 s irradiation and PET data were measured for 20 min immediately after the irradiation. Figure 4.28 shows a reconstructed image of the distribution of the positron emitters, which were produced through fragmentation reactions. The peak position in the PET image is highly correlated to the Bragg peak position.

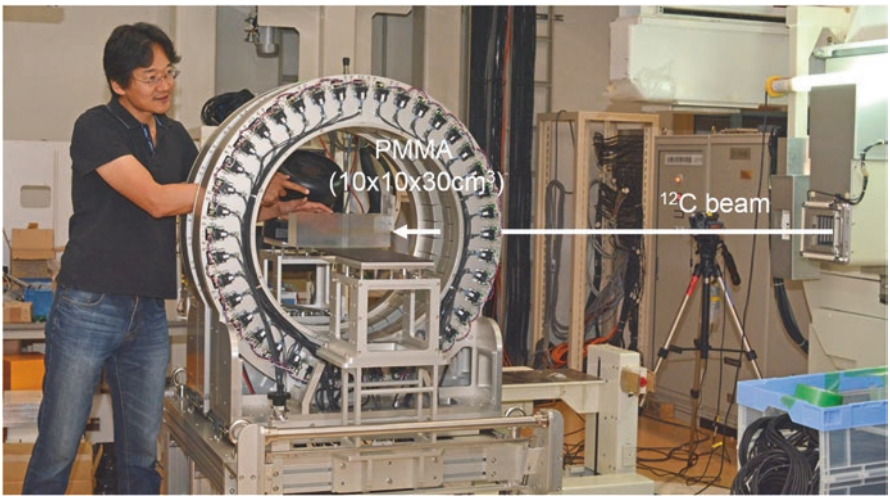

Fig. 4.27 Depicts the in-beam measurement test of ^{12}C beam irradiation at HIMAC

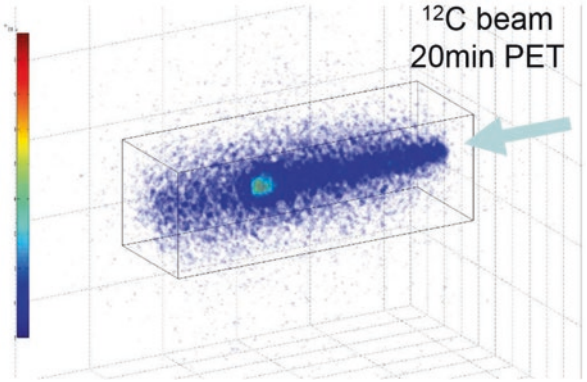

Fig. 4.28 Shows an example of reconstructed DROP images of a PMMA phantom (^{12}C beam irradiation)

4.5 Conclusion

This chapter describes basic concepts and component technologies of our OpenPET systems, which led to the world's first open-type 3D PET scanner. Even with a full-ring geometry, the DROP has an open gap between its two detector rings. The SROP is a more efficient OpenPET geometry in terms of the gap size and the sensitivity. Demonstrations with prototypes showed a proof of concept of PET image-guided particle therapy such as in situ dose verification and direct tumor tracking.

References

1. Carrier C, Martel C, Schmitt D, et al. Design of a high resolution positron emission tomograph using solid state scintillation detectors. IEEE Trans Nucl Sci. 1988;35:685–90.
2. Yamamoto S, Ishibashi H. A GSO depth of interaction detector for PET. IEEE Trans Nucl Sci. 1998;45:1078–82.
3. Wienhard K, Schmand M, Casey ME, et al. The ECAT HRRT: performance and first clinical application of the new high-resolution research tomograph. IEEE Trans Nucl Sci. 2002;49:104–10.
4. Yamashita T, Watanabe M, Shimizu K, et al. High resolution block detectors for PET. IEEE Trans Nucl Sci. 1990;37:589–93.
5. Moses WW, Derenzo SE, Melcher CL, et al. A room temperature LSO/PIN photodiode PET detector module that measures depth of interaction. IEEE Trans Nucl Sci. 1995;42:1085–9.
6. Miyaoka RS, Lewellen TK, Yu H, et al. Design of a depth of interaction (DOI) PET detector module. IEEE Trans Nucl Sci. 1998;45:1069–73.
7. Shao Y, Silverman RW, Farrell R, et al. Design studies of a high resolution PET detector using APD arrays. IEEE Trans Nucl Sci. 2000;47:1051–7.
8. Murayama H, Ishibashi H, Uchida H, et al. Depth encoding multicrystal detectors for PET. IEEE Trans Nucl Sci. 1998;45:1152–7.
9. Inadama N, Murayama H, Omura T, et al. A depth of interaction detector for PET with GSO crystals doped with different amounts of Ce. IEEE Trans Nucl Sci. 2012;49:629–33.
10. Yamaya T, Yoshida E, Obi T, et al. First human brain imaging by the jPET-D4 prototype with a pre-computed system matrix. IEEE Trans Nucl Sci. 2008;55:2482–92.
11. Tsuda T, Murayama H, Kitamura K, et al. A four-layer depth of interaction detector block for small animal PET. IEEE Trans Nucl Sci. 2004;51:2537–42.
12. Miyake K, Matsumoto K, Inoue M, et al. Performance evaluation of a new dedicated breast PET scanner using NEMA NU4-2008 standards. J Nucl Med. 2014;55:1198–203.
13. Yamaya T, Inaniwa T, Minohara S, et al. A proposal of an open PET geometry. Phys Med Biol. 2008;53:757–73.
14. Enghardt W, Crespo P, Fiedler F, et al. Charged hadron tumour therapy monitoring by means of PET. Nucl Instrum Methods Phys Res A. 2004;525:284–8.
15. Pawelke J, Byars L, Enghardt W, et al. The investigation of different cameras for in-beam PET imaging. Phys Med Biol. 1996;41:279–96.
16. Iseki Y, Mizuno H, Futami Y, et al. Positron camera for range verification of heavy-ion radiotherapy. Nucl Instrum Methods Phys Res A. 2003;515:840–9.
17. Parodi K, Pönisch F, Enghardt W. Experimental study on the feasibility of in-beam PET for accurate monitoring of proton therapy. IEEE Trans Nucl Sci. 2005;52:778–86.
18. Nishio T, Ogino T, Nomura K, et al. Dose-volume delivery guided proton therapy using beam ON-LINE PET system. Med Phys. 2006;33:4190–7.
19. Crespo P, Shakirin G, Enghardt W. On the detector arrangement for in-beam PET for hadron therapy monitoring. Phys Med Biol. 2006;51:2143–63.
20. Hudson HM, Larkin RS. Accelerated image reconstruction using ordered subsets of projection data. IEEE Trans Med Imaging. 1994;13:601–9.
21. Yamaya T, Yoshida E, Inaniwa T, et al. Development of a small prototype for a proof-of-concept of OpenPET imaging. Phys Med Biol. 2011;56:1123–37.
22. Hirao Y, Ogawa H, Yamada S, et al. Heavy ion synchrotron for medical use—HIMAC project at NIRS-JAPAN. Nucl Phys A. 1992;538:541–50.
23. Mashino H, Yamamoto S. Development of a compact and flexible data acquisition system for K-PETs. World Congress on Medical Physics and Biomedical Engineering 2006. IFMBE Proc. 2007;14:1722–5.
24. Yamaya T, Hagiwara N, Obi T, et al. Transaxial system models for jPET-D4 image reconstruction. Phys Med Biol. 2005;50:5339–55.

25. Urakabe E, Kanai T, Kanazawa M, et al. Spot scanning using radioactive ^{11}C beams for heavy-ion radiotherapy. Jpn J Appl Phys. 2001;40:2540–8.
26. Parodi K, Crespo P, Eickhoff H, et al. Random coincidences during in-beam PET measurements at microbunched therapeutic ion beams. Nucl Instrum Methods Phys Res A. 2005;545:446–58.
27. Crespo P, Barthel T, Frais-Kölbl H, et al. Suppression of random coincidences during in-beam PET measurements at ion beam radiotherapy facilities. IEEE Trans Nucl Sci. 2005;52:980–7.
28. Tanaka E, Kudo H. Subset-dependent relaxation in block-iterative algorithms for image reconstruction in emission tomography. Phys Med Biol. 2003;48:1405–22.
29. Nakayama T, Kudo H. Derivation and implementation of ordered-subsets algorithms for list-mode PET data. IEEE Nucl Sci Symp Conf Rec. 2005:1950–4.
30. Tashima H, Yoshida E, Kinouchi S, et al. Real-time imaging system for the OpenPET. IEEE Trans Nucl Sci. 2012;59:40–6.
31. Shinaji T, Tashima H, Yoshida E, et al. Time-delay correction method for PET-based tumor tracking. IEEE Trans Nucl Sci. 2014;61:3711–20.
32. Tashima H, Yamaya T, Yoshida E, et al. A single-ring OpenPET enabling PET imaging during radiotherapy. Phys Med Biol. 2012;57:4705–18.
33. Yoshida E, Tashima H, Wakizaka H, et al. Development of a single-ring OpenPET prototype. Nucl Instr Meth Phys Res A. 2013;729:800–8.
34. Tashima H, Yoshida E, Inadama N, et al. Development of a small single-ring OpenPET prototype with a novel transformable architecture. Phys Med Biol. 2016;61:1795–809.
35. Hirano Y, Nitta M, Inadama N, et al. Performance evaluation of a depth-of-interaction detector by use of position-sensitive PMT with a super-bialkali photocathode. Radiol Phys Technol. 2014;7:57–66.